Submesoscale dynamics in tropical instability waves

Patrick Marchesiello [a,*], Xavier Capet [b], Christophe Menkes [c], Sean C. Kennan [d]

[a] IRD, Laboratoire d'Études en Géophysique et Océanographie Spatiale (LEGOS), 14 avenue Edouard Belin, 31400 Toulouse, France
[b] CNRS, Laboratoire de Physique des Océans (LPO), BP 70, 29280 Plouzané, France
[c] IRD, Laboratoire d'Océanographie et du Climat: Expérimentations et approches numériques (LOCEAN), BP A5, 98848, Noumea, New Caledonia
[d] National Science Foundation, Arlington, VA, USA

ARTICLE INFO

ABSTRACT

Submesoscale dynamics in tropical instability waves (TIWs) of the Pacific ocean are analyzed from nested numerical simulations of increasing resolution (36 km, 12 km, and 4 km). It is shown that numerical convergence, as determined by an invariance of the kinetic energy (KE) spectrum with resolution, can be obtained for grid spacing around 10 km. This finding contrasts with mid-latitude simulations of submesoscale processes that do not converge even for grid spacing less than 1 km. The difference is associated with the larger Rossby radius of deformation at low latitudes due to the weaker Coriolis parameter. For the same reason, the mixed layer Rossby radius is larger as well, resulting in submesoscale mixed layer eddies (MLEs) with scales of 50–200 km. Similar to MLEs at mid-latitudes, those eddies that form at TIW fronts restratify the mixed layer by releasing available potential energy. They lead to an additional source of KE at submesoscale that is larger in the finer resolution simulations. At wavelengths smaller than the mesoscale peak of KE injection, a forward cascade of KE is evident in the simulations where three dynamical ranges are observed: a quasi-inertial range of slope k^{-2}, a pre-dissipation range and a far-dissipation range. Numerical dissipation is evaluated and significant dissipation is found to occur in a pre-dissipation range, *i.e.*, for wavenumbers well below the range where the KE spectrum tails off exponentially.

© 2011 Elsevier Ltd. All rights reserved.

1. Introduction

In recent years, understanding of oceanic submesoscale dynamics has significantly improved (see Thomas et al., 2008, for a review). While still investigating its specific role, in particular in biogeochemical transport, we now acknowledge the ubiquity of upper ocean frontal dynamics in many mid- and high-latitude oceanic regions. Because typical scales across surface fronts are well below the deformation radius, this dynamics is called submesoscale. A potentially important aspect of submesoscale dynamics is its role in the energetic functioning of the upper ocean. It often responds vigorously to atmospheric forcing and there is a strong indication that it mediates to some extent the process and quantity of buoyancy, momentum and energy penetration into the deeper ocean. Going beyond our present knowledge requires a better description of submesoscale regimes and understanding of the connection between submeso- and microscales (weakly influenced by earth rotation). This study contributes to both aspects by (i) documenting the type of submesoscale that populates an equatorial region (ii) addressing the issue of frontal statistical arrest (Capet et al., 2008a,c; Taylor and Ferrari, 2009), and particularly, the

convergence of kinetic energy injection associated with frontal intensification and baroclinic instability. The latter is a salient issue because vertical velocities and tracer fluxes are not directly measurable so that their estimation, using prognostic or diagnostic numerical methods, is sensitive to model/data resolution.

The conceptual framework for this study is largely inspired by the works of Capet et al. (2008c), Klein et al. (2008), and Molemaker et al. (2010). The increase of numerical resolution toward the kilometer scale (or improvement of observational data coverage and treatment; Le Traon et al., 2008) invariably leads to flatter surface KE spectra than those expected from quasi-geostrophic mesoscale dynamics: spectral slope is closer to −2 than −3 or steeper. KE injection initiated by mesoscale straining and possibly reinforced by submesoscale instability is the underlying mechanism that produces shallower spectra. Although intensified at the submesoscale, this injection occurs over a broad range of scales where the existence of a true inertial cascade is therefore precluded. Advection nonetheless plays an important role by fluxing KE energy upward from mesoscale to large scale (inverse cascade) and downward to submesoscale (forward cascade). Consequently, part of the kinetic energy released from available potential energy (APE) leaks toward smaller scales, en route to dissipation (Molemaker et al., 2010); in the process, it participates in surface restratification. Although this leakage is presumably important in the upper

* Corresponding author.
E-mail address: Patrick.Marchesiello@ird.fr (P. Marchesiello).

ocean only, remaining uncertainties on the oceanic energy cycle provide a strong motivation for further investigation.

This conceptual framework is consistent with other modeling studies and also with few observational evidences, all of them for mid-latitude regions or idealized situations. To our knowledge, the only energy budget for a non-quasi-geostrophic numerical solution having converged is presented in Molemaker et al. (2010). Dimensionalized for mid-latitudes, frontal arrest occurs in these simulations at a horizontal resolution of about 250 m. Mixed layer instabilities (MLI) that are known to invigorate sub-mesoscale turbulence (Boccaletti et al., 2007) are not permitted in the idealized configuration of Molemaker et al. (2010), but theoretical arguments suggest that their results would hold true using more realistic models. However, since the Coriolis frequency enters the expression for the mesoscale and submesoscale basic eddy lengths (baroclinic and mixed layer deformation radii), we anticipate a shift toward larger values for all other length scales in the problem, in particular the inverse/forward flux separation scale and the resolution required to reach frontal arrest (in a statistical sense). From altimeter data, such a latitude effect on the spectral energy density and flux has been evidenced at mesoscale by Scott and Wang (2005), but no investigation of this effect on the submesoscale spectral energy balance has yet been documented.

The near-equatorial band combines large changes of the Coriolis frequency with intense mesoscale straining due to tropical instabilities. Tropical instability waves (TIWs) are common to the Pacific and Atlantic ocean, routinely observed in space-borne sea surface temperature (SST) as large-scale, westward-propagating oscillations with spatial scales of about 1000 km and propagation speeds of about 30 km d^{-1} (Legeckis, 1986). The origin and characteristics of these large-scale oscillations have been widely studied and represented with success in numerical models (for example, Menkes et al., 2006; Jochum et al., 2007), but the occurrence and dynamics of sub-wave (submesoscale) structures have long been neglected by modelers. Yet, there is clear observational evidence of frontal dynamics showing intense convergent fronts with large values and asymmetric distribution of vertical velocity and vorticity (Johnson, 1996; Flament et al., 1996; Kennan and Flament, 2000). The simulation of such small-scale phenomena in high resolution models of the tropical Pacific faces new challenges regarding, in particular, the resolution needed in models to fully capture the submesoscale dynamics and their effect on equatorial upwelling oceanography. This problem is particularly relevant to the series of observations detecting a spectacular *line in the sea* (Yoder et al., 1994; Murray et al., 1994, and references therein) of concentrated buoyant phytoplankton at the convergent front of tropical instability waves.

In this paper, the submesoscale-resolving model used in a mid-latitude region by Capet et al. (2008c) is applied to the near equatorial region of central Pacific where tropical instability waves are generated (Section 2). A suite of model solutions with increasing resolution confirms a shift toward larger scales of the KE spectrum and reveals the presence and effect of submesoscale activity that experiences this shift (Section 3). Consequences for high-resolution, submesoscale modeling are then discussed.

2. Model and configurations

The Regional Oceanic Modeling System (ROMS; Shchepetkin and McWilliams, 2005) is used here in its version with two-way nesting capability (ROMS-AGRIF; Penven et al., 2006; Debreu et al., 2011). ROMS is a split-explicit, free-surface and terrain-following vertical coordinate oceanic model. Its finite-difference discretization methods have been specially designed for optimizing

the resolution of small-scale processes. A modified Adams–Moulton-3 predictor–corrector time-step algorithm allows a third-order accurate time-stepping with substantial increase in the permissible time-step size; in combination with third-order time stepping, an upstream-biased, dissipative advection scheme for momentum allows the generation of steep gradients in model simulations, enhancing the effective resolution of the solution for a given grid size (Shchepetkin and McWilliams, 1998). Explicit lateral viscosity is null everywhere in the model, except in sponge layers near the open boundaries where it increases smoothly on several grid points. For tracers, a fourth-order centered scheme is used along with rotated hyperdiffusivity, to avoid excessive spurious diapycnal mixing in the sigma coordinates framework (Marchesiello et al., 2009). A K-profile parameterization (KPP) boundary layer scheme (Large et al., 1994) parameterizes the subgrid-scale vertical mixing processes.

To represent TIWs at various resolutions, multiple embedded grids with two-way communication are configured, starting from a full tropical Pacific domain at 1° resolution. The grid refinement rate at each level is 3 so that grid resolutions are 1/3°, 1/9° and 1/27° (36 km, 12 km and 4 km resolution in the TIWs area). With two-way nesting, the parent grid solution is updated from the child allowing smooth, continuous interfacing between grid levels. However, as opposed to one-way nesting, the updated parent solution has no intrinsic value in the refinement area and cannot be used for estimating resolution sensitivity. Instead, coarser simulations must be conducted with increasingly fewer refinement levels; here three simulations of variable resolution are proposed:

- FINE: 4 km resolution grid encompassing one selected TIW, embedded into 3 coarser grids.
- MEDIUM: 12 km resolution grid encompassing three TIWs, embedded into 2 coarser grids.
- COARSE: 36 km resolution grid encompassing the main TIW formation area, embedded into the 1° resolution grid.

The resolution sensitivity (at 4 km, 12 km and 36 km resolutions) serves as a measure of the convergence level of the model solution. The 1° resolution grid is not used for comparison as it is too coarse for proper spectral diagnostics to be made (a few grid points per wave). The model grids, forcing, initial and boundary conditions are built using the ROMSTOOLS package (Penven et al., 2008). The bottom topography is derived from a 2' resolution database from NOAA-NGDC (ETOPO2). Although pressure gradient errors in ROMS are handled by a high-order scheme (Shchepetkin and McWilliams, 2003), bathymetry smoothing that maintains a upper limit of 0.2 for the slope parameter $\Delta h/2h$ is still needed. In any case, the bathymetry in the eastern equatorial Pacific is naturally smooth and flat and does not play any significant role in our analysis. To preserve a sufficient resolution in the upper ocean, we use 30 vertical levels with surface-stretched s-coordinates (parameters $\theta_s = 6$, $\theta_b = 0$). The surface layer resolution is about 5 m and a maximum grid size of about 500 m is in the bottom layer.

The model external forcing is derived from global model reanalysis, simulations, and satellite observations. At the surface, the model heat and fresh water fluxes are extracted from the COADS climatology (da Silva et al., 1994). Momentum fluxes are interpolated from the weekly wind stress product derived from the ERS satellite scatterometer data, provided by CERSAT (www.ifremer.fr/cersat) on a 1° grid for the period 1993–2000. At the three lateral boundaries facing the open ocean, a mixed passive-active radiation condition connects the model solution to the surroundings (Marchesiello et al., 2001). In the case of inflow conditions, the solution at the boundary is nudged toward monthly outputs of the ORCA05 global ocean model, which was run on a 1/2° resolution grid for the period 1992–2002 (Couvelard et al., 2008).
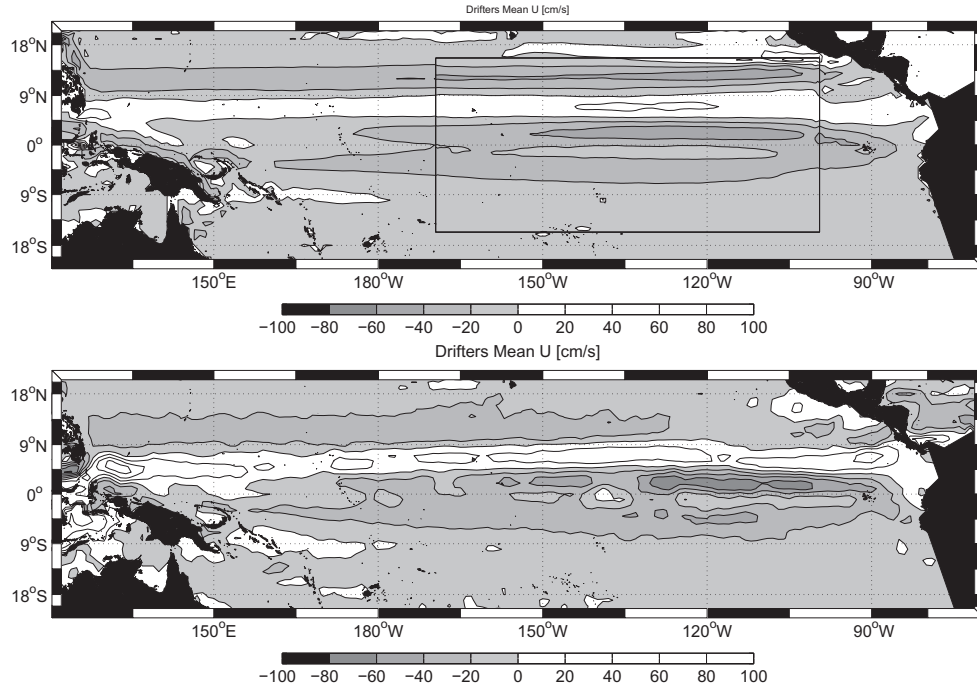
Fig. 1. Mean surface zonal velocity (cm s^{-1}). Top: 1993–2000 Mean U from ROMS COARSE solution (36 km resolution grid in the TIW region nested into a 1° grid). Bottom: drifter observation (R. Lumpkin, personal communication); the drifter data was low passed at 5 days to remove inertial and tidal motion; the data density is relatively high in the TIW region.

Finally, initial conditions in the FINE, MEDIUM and COARSE simulations are interpolated from the equilibrated 1° model solution after about six years of spin up (1993–1998) starting with ORCA05 January mean values. The analyses are performed using three month long simulations starting from September 1998 (hereafter noted 'high TIW season'), *i.e.*, during the 1998 La Nina event. During the three month period, three TIWs were able to cross the finest grid domain.

3. Results and analyses

3.1. Equatorial dynamics and mesoscale structure

A complete model verification of equatorial dynamics and TIW activity is beyond the scope of this paper which is devoted to the submesoscale. However, submesoscale dynamics partly results from straining by mesoscale eddies, which thus require a minimum validation. 1993–2000 mean characteristics of equatorial dynamics are presented for the COARSE solution[1] in Figs. 1–4, where they are compared with drifter estimations (Lumpkin and Garraffo, 2005) and TOGA-TAO current observations (McPhaden and McCarty, 1992). The mean equatorial current system is composed of the eastward flowing North Equatorial Counter-Current (NECC) and Equatorial Undercurrent (EUC), and the westward flowing South and North Equatorial Currents (SEC and NEC). They are represented in the model with realistic structure and magnitude within uncertainties of wind forcing sensitivity (Cravatte and Menkes, 2009). The EUC at 140°W and 110°W compares well with both TAO mooring observations and other models (Vialard et al., 2001), although it appears about 20 m too deep at 110°W (a bias expected with ERS wind forcing; see Cravatte and

Menkes, 2009). The realistic model representation of mean horizontal and vertical flow shears is also associated with realistic mean Eddy Kinetic Energy (EKE) along the equatorial guide compared to drifter observations (Fig. 4); large EKE values are found all along the equator with maximum values in the eastern equatorial Pacific (TIW region). The model EKE generation is related to both barotropic and baroclinic conversions. Fig. 5 presents the time-mean baroclinic and dominant barotropic conversion terms, respectively $\overline{w'b'}$ and $-\overline{u'v'}\frac{\partial \bar{u}}{\partial y}$ ($-\overline{v'v'}\frac{\partial \bar{v}}{\partial y}$ is not negligible at the surface but has only weak vertical extent). Barotropic conversion is composed of narrow bands of large values, *i.e.*, a primary band near the equator (in the region of shear between EUC and SEC) and a secondary band around 4°N (in the region of shear between SEC and NECC); baroclinic conversion presents a broader pattern between the equator and 6°N. These results are similar to those presented by Masina et al. (1999) and consistent with drifter estimations by Baturin and Niiler (1997). The same approximate ratio of 3/2 for barotropic/baroclinic conversion as Masina et al. (1999) is also found here.

Fig. 6 shows the embedded solution when all nested grids are used. It represents a snapshot of sea surface temperature during October 1998. All the known features of the tropical Pacific Ocean are present, *i.e.*, the warm pool in the west and the cold tongue in the east extending from the coast of Peru and producing a westward-propagating tropical instability wave train. TIWs are associated with anticyclonic tropical instability vortices (TIVs; Kennan and Flament, 2000) evidenced on sea surface height in Fig. 7. In the model as in nature, TIW activity is strongest during boreal summer and autumn and are enhanced during La Nina periods, as in 1998. The model TIWs characteristics are consistent with general observations (Willett et al., 2006): TIW wavelength is about 1000 km while TIV size is about 500 km, located between 2°N and 8°N (*in situ* observations of a vortex is presented in Fig. 9 and commented in the next section), and travelling westward at about 30 km d^{-1}; their wave period at the equator is in the range 15–40 days as in TAO moorings (Fig. 3; see Lyman

---

[1] MEDIUM and FINE solutions were only integrated over 3 months and thus cannot be used for estimation of mean properties. However, our resolution comparison in Section 3.5 will show that mesoscale energy is not very sensitive to further increase of resolution from COARSE.
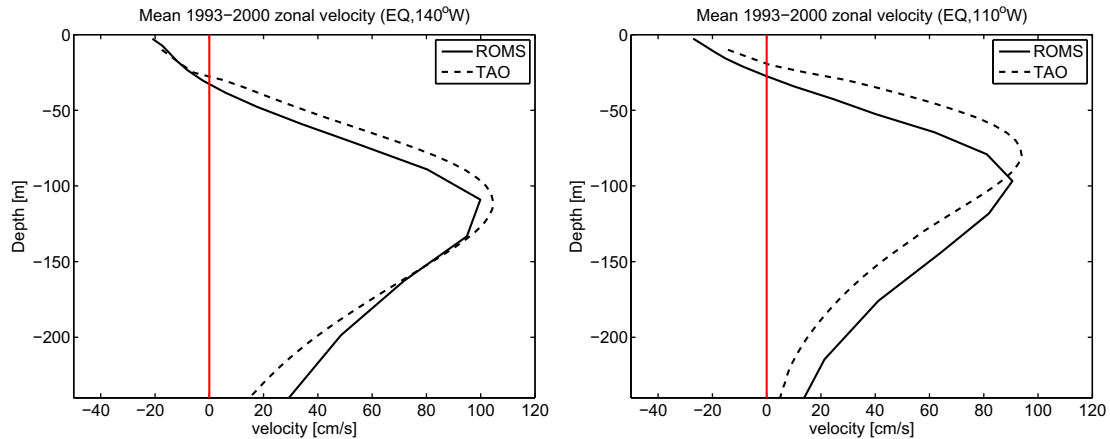
Fig. 2. Mean 1993–2000 zonal current profiles of ROMS (COARSE solution) and TAO data at two moorings (140°W and 110°W at the equator). Units are cm s^{-1}.
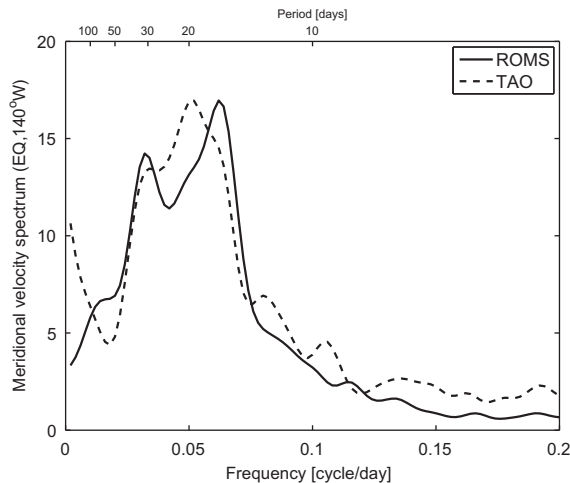
Fig. 3. Frequency spectra of surface meridional velocity in ROMS (COARSE solution) and TAO data at moorings (EQ, 140°W); In both cases, the peak amplitudes correspond to a range of periods of 15–40 days.

et al., 2007, for details about the equatorial frequency spectrum). In TIWs, the cusps of the SST front is due to northward advection, on the leading edge of TIVs, of cold water from the equatorial upwelling zone. Peak currents on this edge exceed 1.5 m s^{-1}. TIVs are also associated with a depression of the thermocline of about 50 m.

3.2. Submesoscale structure

In all simulations (FINE, MEDIUM and COARSE), TIWs and TIVs are represented with similar wave scale (or *mesoscale*) characteristics. The main differences arise at frontal scale (*submesoscale*). This is clearly illustrated in Fig. 8 showing that a simulated TIW can have the same location and mesoscale structure in all 3 simulations, *i.e.*, the TIW can travel through 2 nested interfaces without alteration of its wave properties.[2] Fig. 8 presents comparisons of FINE, MEDIUM and COARSE solutions for SST, surface vertical vorticity ξ, 10 m vertical velocity w and submesoscale temperature flux $w''T''$. w'' and T' are submesoscale perturbations of the vertical

velocity and temperature fields; they are computed as the difference between total and low-pass filtered components (Capet et al., 2008a). The low-pass filter is a combination of temporal averaging over 3 days and horizontal smoothing with a 50 km decorrelation radius, removing frontal scales.

All fields at all resolutions indicate strong frontogenesis resulting from straining in the vicinity of TIVs. Frontal dynamical features (in particular, asymmetry of vertical velocity and vertical vorticity) appear as predicted by the semigeostrophic theory of frontogenesis (Hoskins, 1982; Thomas and Lee, 2005): downward velocities on the cold side of fronts (maxima near -100 m d^{-1}) are much stronger than upward velocities on the warm side (maxima around 40 m d^{-1}); cyclonic vorticity on the cold side is much stronger than anticyclonic vorticity on the warm side (due to asymmetry of vortex stretching/squashing $\sim (f + \xi)\frac{\partial w}{\partial z}$ across the front); vertical heat flux is positive on both sides of the front but much stronger on the cold side. The frontal w pattern is attributed to the ageostrophic secondary cross-frontal circulation which attempts at restoring geostrophic balance and also results from the divergence of Ekman transport affected by frontal vorticity changes (Stern, 1965; Niiler, 1969).

The kinematics of model TIVs are also in general agreement with *in situ* observations (Johnson, 1996; Flament et al., 1996; Kennan and Flament, 2000). Fig. 9 presents surface velocity and vorticity observations from the second cruise of the 1990 Tropical Instability Wave Experiment (TIWE-2; Kennan and Flament, 2000). This gridded (at 1/4° resolution) quasi-synoptic observation (sampled over ~20 days and mapped using a translating frame to recover the vortex coherence) is smooth but reveals an anticyclonic vortex of about 500 km with speeds approaching 1 m s^{-1}. As in the model (Fig. 8, second row), relative vorticity is intense (compared to f) with anticyclonic values in the vortex core (where absolute vorticity approaches zero) and mostly cyclonic values on the edges. Note in particular the filament of high positive vorticity along the leading edge of the vortex, similar to the model solution and consistent with frontogenesis theory.

If frontogenesis is obvious at all model solutions, submesoscale meanders and eddies are clearly present only in the MEDIUM and FINE solutions. In the FINE solution, these submesoscale phenomena are more vigorous and, interestingly, most noticeable away from the major straining area in the northern zone between 4°N and 8°N where they seem capable of breaking up forming filaments at the edge of TIVs. Traces of such submesoscale perturbation in the northeast corner of the vortex are also noticeable in the TIWE data (Fig. 9).

---

[2] Contrarily to 1-way nesting (online or offline with open boundary conditions), 2-way nesting has a much better interface behavior, provided that a proper treatment is given to conservation and update issues (Debreu et al., 2011, for a complete description of the method).
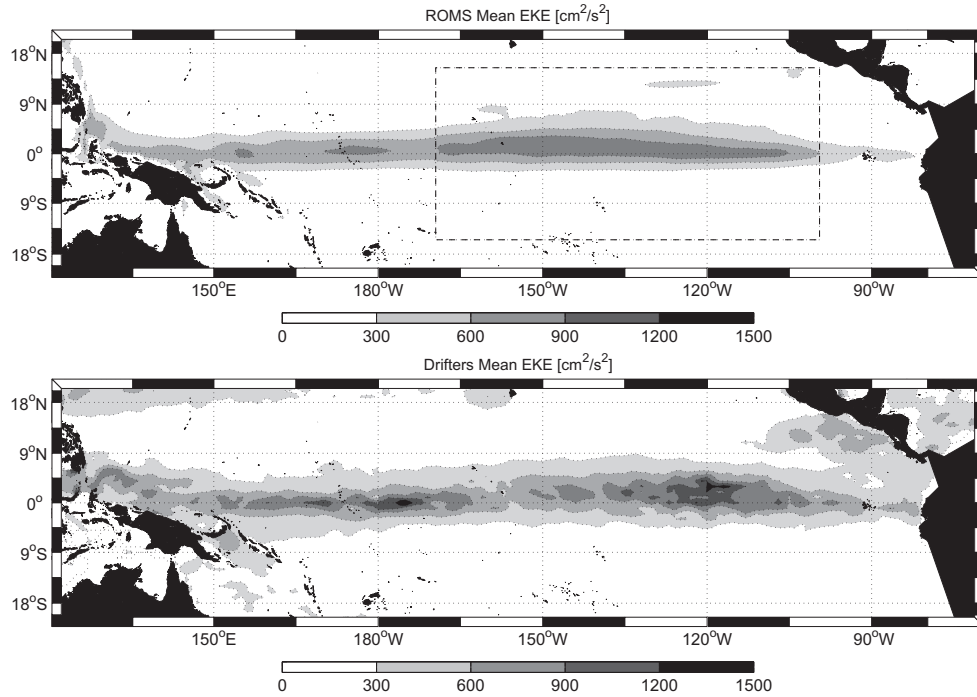
Fig. 4. Mean surface Eddy Kinetic Energy (cm^2/s^2). Top: 1993–2000 Mean EKE from ROMS COARSE solution (36 km resolution grid in the TIW region nested into a 1° grid). Bottom: drifter observation (R. Lumpkin, personal communication); the drifter data was low passed at 5 days to remove inertial and tidal motion; the data density is relatively high in the TIW region.
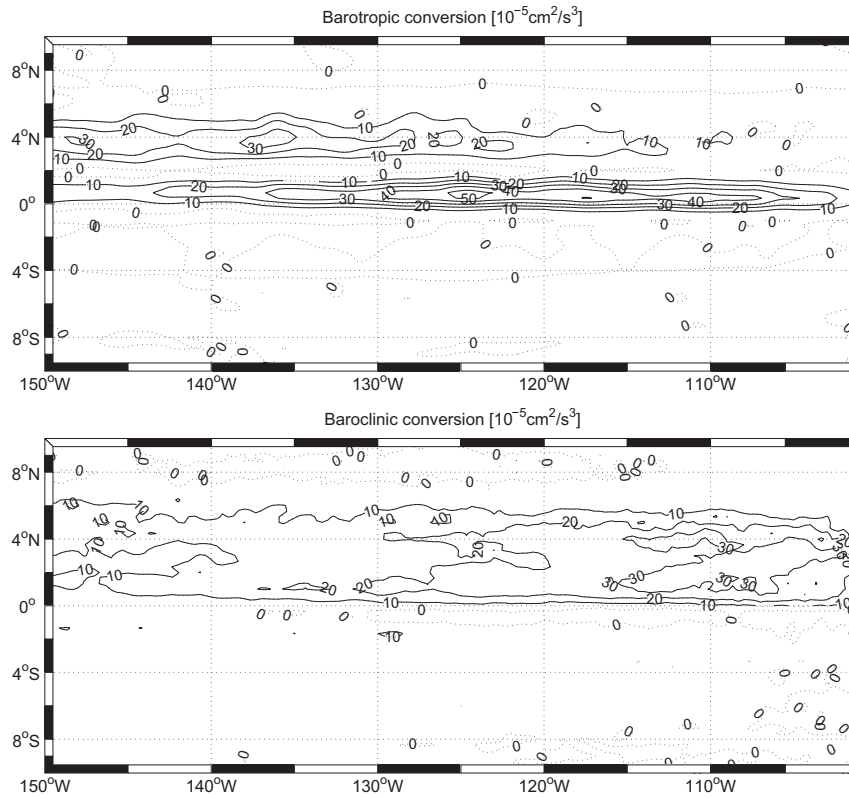
Fig. 5. EKE conversion at 10-m depth in the COARSE solution (in units of 10^{-5} cm^2/s^3; dashed lines represent negative values). Top: barotropic conversion from mean to eddy kinetic energy $-\overline{u'v'}\frac{\partial \bar{u}}{\partial y}$. Bottom: baroclinic conversion from available potential energy $\overline{w'b'}$. Eddy flow refers here to all perturbations of the 1993–2000 time mean flow except for temporal scales of less than a day which have been filtered. The other barotropic conversion terms are much smaller that the one presented in the top panel (only the term $-\overline{v'v'}\frac{\partial \bar{v}}{\partial y}$ can locally reach significant values), consistent with Masina et al., 1999.

ROMS surface temperature
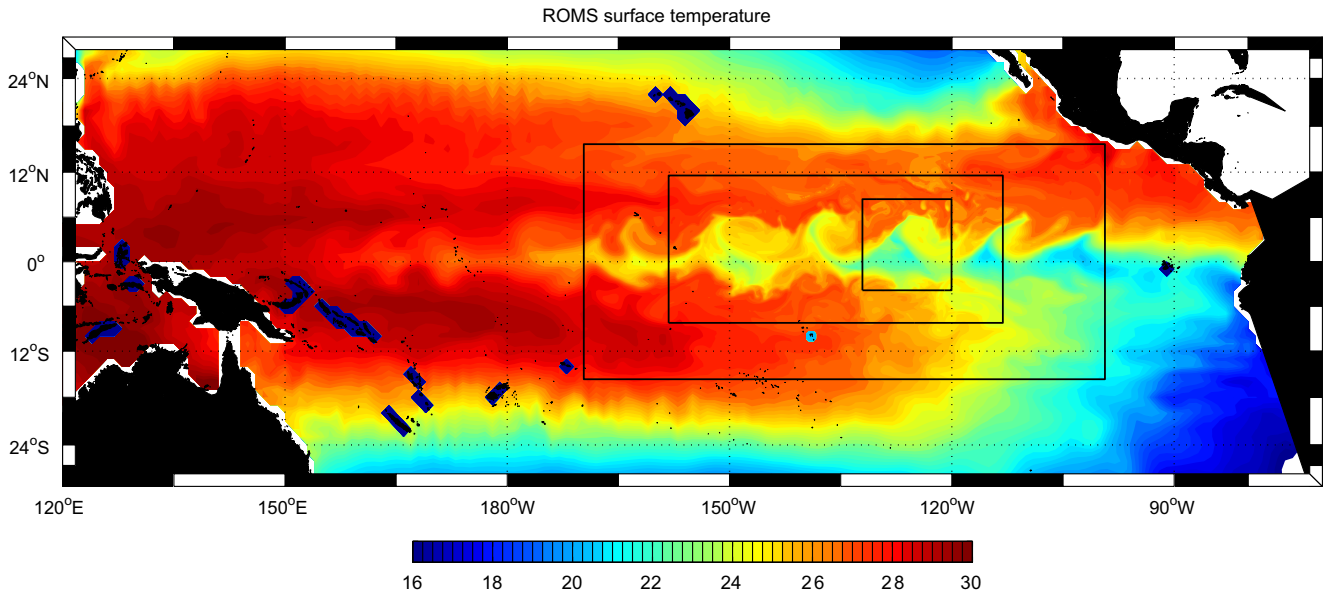
Fig. 6. ROMS SST simulation in November 1998 from the four embedded grid configuration (FINE model solution). The limits of the 2-way nested domains are represented by rectangles.

ROMS sea level (cm)
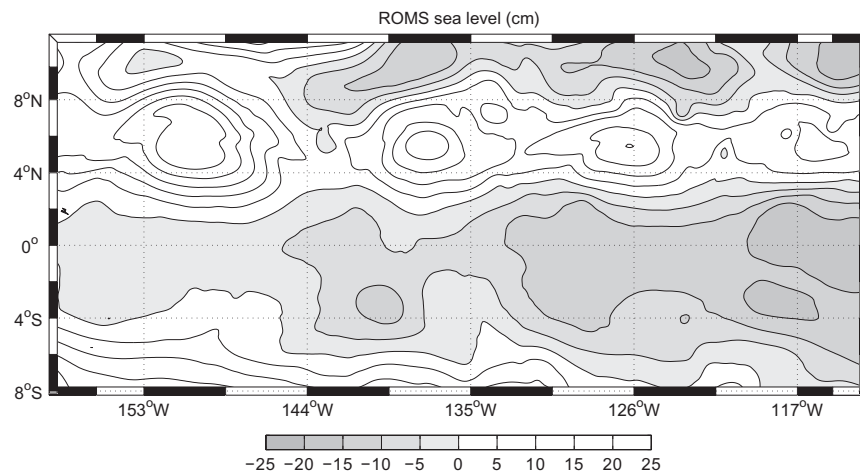
Fig. 7. Model surface elevation in November 1998 from the MEDIUM solution. Units are cm.

3.3. Kinetic energy spectrum

Much insight into submesoscale dynamical regimes can be gained by exposing its energy spectral characteristics.[3] Fig. 10 shows shell-integrated two-dimensional KE spectra as a function of the horizontal wavenumber magnitude (Capet et al., 2008c, for details on the method). The MEDIUM domain area is used for this spectral analysis (which corresponds to about 400×200 grid points); Areal mean is removed and KE fields are made periodic by symmetrization (Denis et al., 2002) to allow the Fourier analysis of our regional non periodic signals; 90 fields at daily intervals are processed to obtain an average spectrum. Since the domain of analysis encompasses the size of a tropical instability wave (in the meridional direction), the largest scales that are retained in our analysis represent the TIW (meso) scale. The spectrum in classical log–log scale (top panel) decays approximately linearly with a slope shallower than -3 until it strongly decays near the grid scale. A compensated spectrum for a k^{-2} power law ($KE(k)$ multiplied by k^2) is shown in the bottom panel of Fig. 10. There is an obvious peak of energy around 1000 km which corresponds to the TIW wavelength. Then, it is evidently flat in the scale range between 500 and 200 km with a steeper decay at smaller scales. The energy budget underlying this spectrum shape is presented in the next section in ways that will expose the location and transitions between mesoscale, submesoscale and dissipation regimes. The sensitivity of KE budget to resolution will also expose the convergence properties of the model.

3.4. KE injection, transfer and dissipation

Following Capet et al., 2008c, we produce a spectral decomposition with respect to horizontal wavenumber of the KE balance for the primitive equations, i.e., we compute and combine co-spectra between velocity and the various terms that enter the momentum equations. As for the computation of power spectra above, the areal mean is removed and symmetrization is performed on each term before the Fourier transform is calculated. The dominant terms of the KE budget at submesoscale are: the conversion of potential to kinetic energy I which represents a local injection of KE; advection A (the horizontal term tends to dominate over the vertical one); and dissipation D (lateral and vertical subgrid-scale mixing). The contribution of 3D pressure work P is most important at TIW scale where

---

[3] Advantages and limitations of the spectral approach to the study of turbulence are given in Davidson (2004).
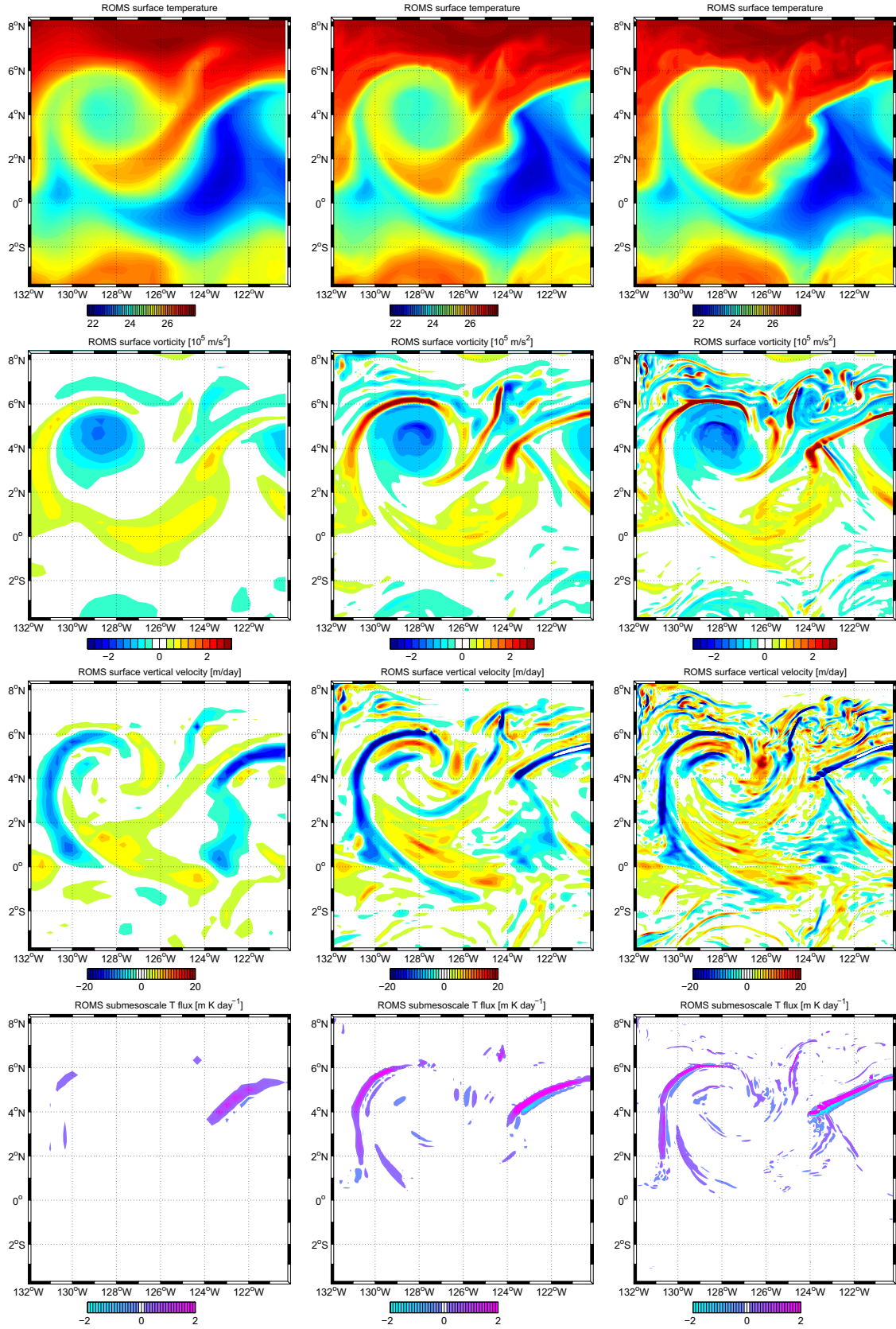
Fig. 8. SST (top row), surface vorticity (second row), 10-m vertical velocity (third row) and 10-m submesoscale vertical T flux (bottom row) in October 1998 (high TIW season) over the area limited by the finest nested domain. The right, center and left columns present respectively the COARSE (36 km), MEDIUM (12 km) and FINE (4 km) solutions.
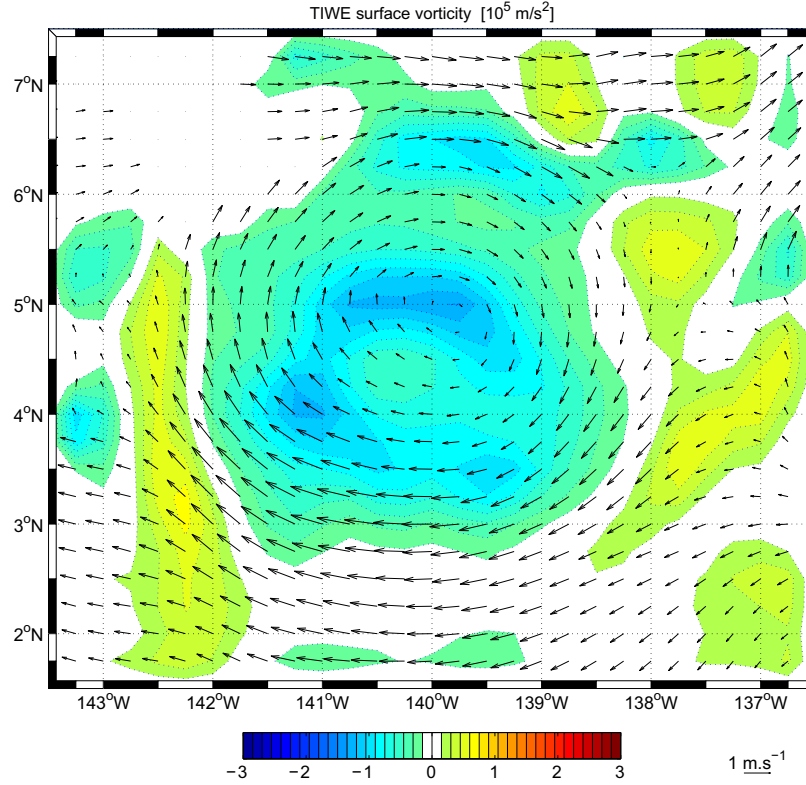
Fig. 9. TIV surface vorticity and velocity observations from the second cruise of the 1990 Tropical Instability Wave Experiment (TIWE-2; Kennan and Flament, 2000). The gridded data at a horizontal resolution of 1/4° is based on all available velocity data (ADCP and drifters) sampled over ~20 days and mapped using a translating reference frame to recover the vortex coherence; note that some values are missing in the northeast corner of the plot. This figure is to be compared with Fig. 8 (second row) for the model.

anticyclonic TIVs redistribute surface KE downward by mesoscale vortex stretching (a process also responsible for thermocline deepening). The sum of all terms (sources, sinks and spectral fluxes) contributes to the time tendency term T which is also only important at the mesoscale level in the three-month average. The spectral KE budget is expressed as:

$$T(k) = P(k) + I(k) + A_H(k) + A_V(k) + D_H(k) + D_V(k),\tag{1}$$

$$I(k) = \Re[\widehat{w^* \widehat{b}}],\tag{2}$$

$$A(k) = A_H(k) + A_V(k) = \Re\left[-\widehat{\mathbf{u}_h^*} \cdot \widehat{(\mathbf{u}_h \cdot \overrightarrow{\triangledown})\mathbf{u}_h} - \widehat{\mathbf{u}_h^*} \cdot \widehat{w \frac{\partial \mathbf{u}_h}{\partial z}}\right],\tag{3}$$

$$D_H(k) = A_H^{UP3} - A_H,\tag{4}$$

$$D_V(k) = \Re\left[\widehat{\mathbf{u}_h^*} \cdot \widehat{\frac{\partial K_V \frac{\partial \mathbf{u}_h}{\partial z}}{\partial z}}\right],\tag{5}$$

$$P(k) = \Re\left[-\frac{1}{\rho_0}\widehat{\mathbf{u}^*} \cdot \widehat{\overrightarrow{\triangledown p}}\right],\tag{6}$$

where b is buoyancy ($=-g\rho/\rho_0$) and K_V is vertical viscosity. The caret denotes a horizontal Fourier transform after removing the areal mean and performing the symmetrization which has the effect of suppressing the advective horizontal fluxes through the lateral boundaries. The asterisk notation $*$ indicates the complex conjugate operator; the symbol $\Re$ represents the real part operator; the overbar represents an average in time over the high TIW season (90 days) and in depth over the average depth of the surface boundary layer (40 m). The momentum advection scheme of the model is third-order upwind which can be split into a non-dissipative, fourth-order, centered scheme and a biharmonic dissipation term with velocity-dependent hyperviscosity (Marchesiello et al., 2009).

Therefore, the lateral mixing term D_H is the difference between advection terms A_H^{UP3} and A_H, computed respectively by the upwind and centered discretization schemes.

The advection terms account for both spectral energy transfer and energy flux through the domain. The lateral flux is cancelled by the periodization method used to compute the spectra and the vertical flux is small. Spectral KE transfer between wavenumbers is thus the essential process accounted for by the advection terms. It is computed as the energy transfer rate in k space, which is the integral in k of the advective term of the KE balance, assuming the flux vanishes at the highest wavenumber k_{max}:

$$\Pi(k) = \int_k^{k_{max}} A\,dk.\tag{7}$$

Fig. 11 (top panel) presents the KE budget terms I, A, D_H, D_V, and P for the MEDIUM resolution in the high TIW season (note that D_H is multiplied by 10 to allow visualization of the dissipation range in the same plot). As previously noted for mid-latitude solutions, KE injection is present on a wide range of scales and largely counteracted by vertical dissipation (Capet et al., 2008c). In the present case, injection is comparatively more concentrated around the $\lambda = 600$ km wavelength, *i.e.* about half the Rossby deformation wavelength. This is consistent with baroclinic instability analysis (Scott and Wang, 2005; Smith, 2007; Tulloch et al., in press), which shows that the scale of the fastest growing mode at low latitude is smaller than the deformation scale within a factor of two (possibly as a result of the thermocline sloping up toward the equator). Observations also suggest that the injection scale is about half the eddy scale at low latitude (Tulloch et al., in press), which is confirmed in our simulations. A difference with mid-latitude dynamics is that the wind work (included in D_V) provides a net KE input at
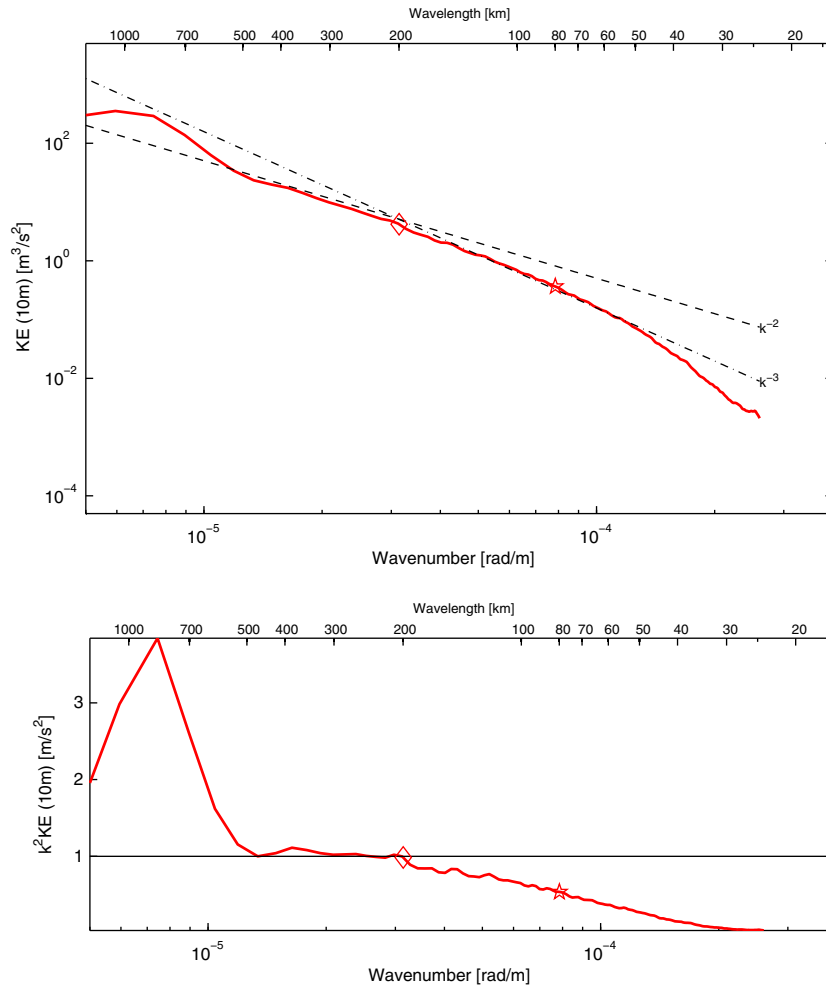
Fig. 10. Top: two-dimensional KE spectrum of MEDIUM solution (12 km) for the horizontal velocity fluctuations at 10 m depth as a function of horizontal wavenumber magnitude (corresponding wavelengths are indicated on top); the straight lines indicate −2 (dashed) and −3 (dot-dash) spectrum slopes. Bottom: compensated spectrum (multiplied by k^2) with a linear ordinate scale. In both panels, the diamond symbol marks the location where the model spectrum first begins to decay relative to a −2 slope, and the star symbol marks the start of a more rapid tail off; these spectral locations may be interpreted as the limits of pre- and far-dissipation subranges (see text).

TIW scale as noted, for example, by Baturin and Niiler (1997) and Scott and Xu (2009).[4] However, in our simulations the surface input is largely compensated by 3D pressure work which radiates this energy below the surface (Masina et al., 1999; Luther and Johnson, 1990). Note that, over the 3 month study period, there was a small loss of KE (negative T) at TIW scale (not shown), which nearly closes the budget. The residual is largest at TIW scale (on the order of the time tendency) and is due to numerical approximations of the offline KE budget and spectral leakage; this residual becomes very small at submesoscale.

The bottom panel of Fig. 11 presents the KE transfer rate $\Pi(k)$. As for mid-latitude cases, $\Pi(k)$ is negative at mesoscale (upward or inverse) and positive at smaller scale (forward toward the dissipation range). The change of sign of energy flux, *i.e.,* the $\Pi(k)$ zero crossing, occurs at wavelength ~600 km. Here, more clearly than at mid-latitude, the separation scale between forward and inverse KE flux corresponds to that for the center of KE injection. This result is consistent with altimeter estimations of $\Pi(k)$ zero crossing at various latitude (Scott and Wang, 2005). However, contrarily to mid-latitude examples, barotropic instability plays an important role in

tropical regions (see 3.1 and Fig. 5). In terms of spectral budget, barotropic instability should provide a contribution to $\Pi(k)$ between the mean flow and eddy scales (Scott and Wang, 2005), *i.e.,* at scales larger than ~1000 km. This range is poorly represented in our regional analysis and further investigation will be needed to isolate the precise role of barotropic instabilities. In any case, a large part of the mesoscale energy travels down to the submesoscale range, where the transfer rate $\Pi(k)$ reaches a plateau. This plateau indicates the existence of an inertial regime (constant energy flux through that wavenumber range), although not as a (usual) consequence of null KE injection and dissipation, but rather of compensation between them. This is again in contrast with mid-latitude cases for which no clear KE flux plateau is obtained even at horizontal resolution ~1 km.

The KE budget analysis leads to an interpretation of the KE spectra. Wind work, baroclinic and barotropic conversions dominate over dissipation at scales larger than 600 km. Then, spectral KE fluxes tend to redistribute energy across wavenumbers and prevent accumulation over the wavenumber range corresponding to the energy source. Part of the energy injection around 600 km follows an inverse cascade toward the eddy scale ~1000 km (consistent with suggestions by Smith (2007), that mesoscale eddies result from energy cascading up from the injection scale). Down from 600 km, and more clearly from 300 km, an inertial-like forward cascade

---

[4] In fully coupled oceanic and atmospheric models, the momentum flux may reverse sign at TIW scale, *i.e.,* the atmosphere may reduce the growth of TIWs by adjusting its wind response to the evolving TIWs (Seo et al., 2007).
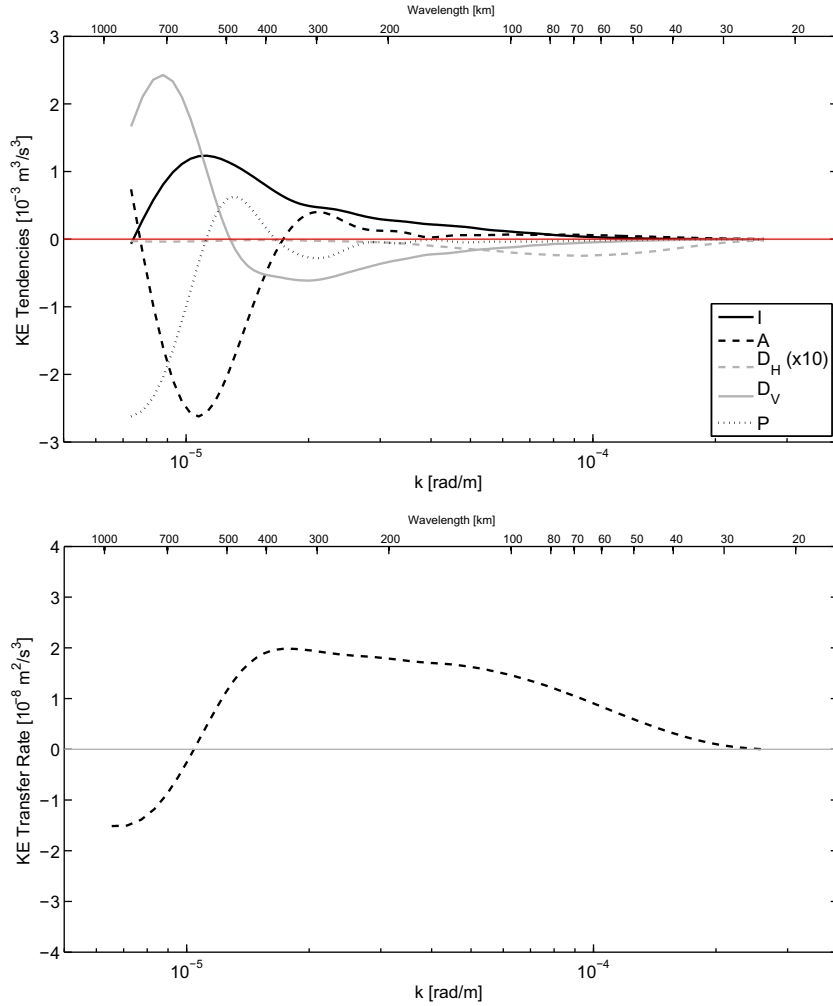
Fig. 11. Top: spectra of KE tendency terms (in units of 10^{-3} m^3/s^3) for injection (I), advection (A), lateral dissipation (D_H), vertical dissipation (D_V) and 3D pressure work (P) defined by Eqs. (2)–(6); all terms are averaged from the MEDIUM solution over the TIW season and the mixed layer (-40 m to the surface); Bottom: spectrum of KE transfer rate Π defined by Eq. (7) (in units of 10^{-8} m^2/s^3).

(plateau of Π) sets in approximately where the KE spectrum decays as k^{-2}. In this regime, KE injection is compensated by vertical dissipation[5] so that any change in I is accompanied by a similar change in D_V and A remains comparatively smaller than either term. Below 200 km and more strongly below 100 km, this inertial-like cascade is broken as the model lateral dissipation becomes an active player ($I + A \sim D_V + D_H$) and prevents any KE accumulation at the grid scale (KE transfer is numerically stopped; Π decreases). The succession of dynamical regimes described here are similar to the mid-latitude case, but with a spectral shift towards larger scales.

3.5. Resolution convergence

The FINE domain area is now used to study the resolution sensitivity of the spectral KE budget. This domain corresponds to about 330^2 grid points (3^2 times less at each new resolution for the MEDIUM and COARSE solutions). Because of the smaller size of the domain, the analysis now contains fewer TIW events (3 instead of about 10) and spectral leakage, despite the periodization function, is larger at the TIW scale. Nevertheless, the main spectral characteristics described in the previous section are retained and

the spectral convergence demonstrated below is deemed meaningful.

Fig. 12 shows the 10 m KE spectra of all three solutions (KE is larger at 10 m than in a mixed layer average but the spectra are qualitatively very similar). The main result of this comparison is the apparent resolution convergence of the spectral KE distribution. Energy increases with resolution in the submesoscale range but mesoscale energy remains nearly constant. In particular, the MEDIUM and FINE spectra cannot be easily distinguished for $\lambda > 100$ km; the increase of resolution from $\delta x = 12$ km to 4 km only seems to extend the range over which KE spectra are straight (in log scales) by displacing the dissipative range of the model toward smaller scales. The compensated spectra (bottom panel) provides additional details. The COARSE solution has the least energy at all scales and shows no k^{-2} regime. The k^{-2} regime in MEDIUM is less clear than in Fig. 10, perhaps as a result of poor statistical representation or spectral leakage around 500–400 km. Nevertheless, the same transition to a dissipative regime is seen at around 200 km (where the budget is more robust). In the FINE solution, the flat spectral range is well represented and extends further to about 100 km.

Again, spectral convergence appears more clearly than in mid-latitude submesoscale solutions (even when going from 1.5 to 0.75 km horizontal resolution in the case of Capet et al. (2008c)). The spectral shift is *a priori* consistent with horizontal length

---

[5] The energy balance between injection and vertical dissipation can be associated with the need for friction to balance cross-frontal Coriolis acceleration due to the ageostrophic circulation (Garrett and Loder, 1981).
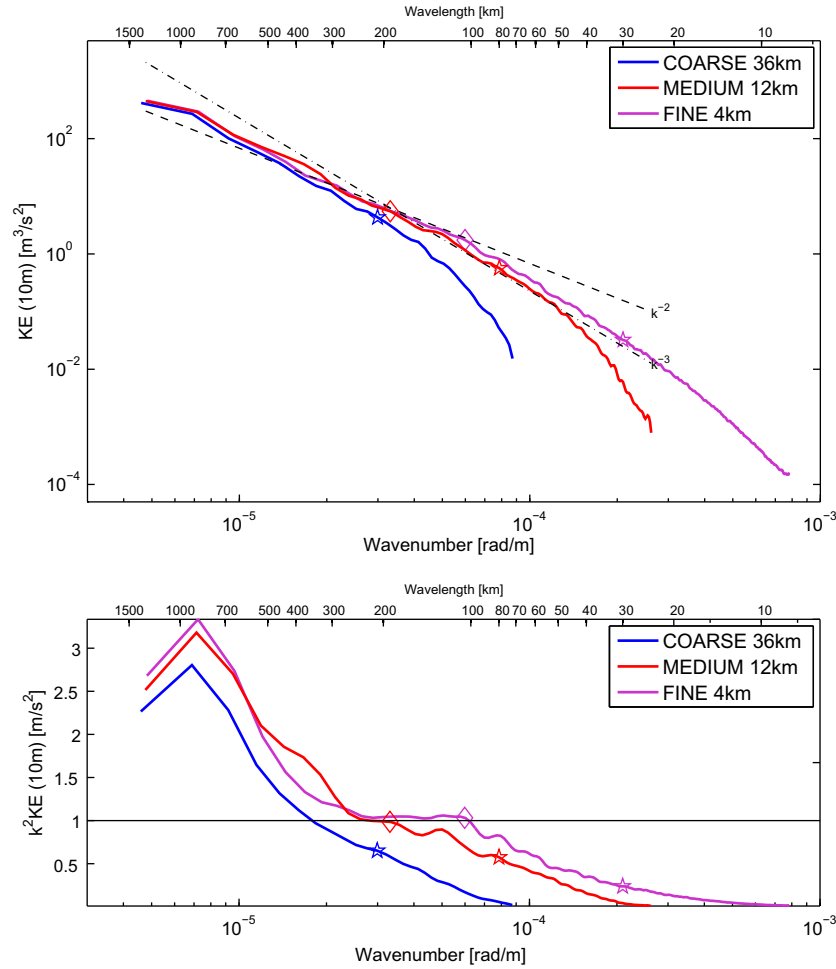
Fig. 12. Two-dimensional KE spectra for the horizontal velocity fluctuations at 10 m depth as a function of horizontal wavenumber magnitude (corresponding wavelengths are indicated on top). The three solid lines correspond to spectra for the different simulations with the wave number range increasing from COARSE to MEDIUM and FINE. (*i.e.*, horizontal grid scale decreasing from 36 km to 12 km and 4 km). The straight lines indicate −2 (dashed) and −3 (dot-dash) spectrum slopes. Bottom: compensated spectrum (multiplied by k^2) with a linear ordinate scale. In both panels, the diamond symbol marks the location where the model spectra first begin to decay relative to a −2 slope (in the FINE and MEDIUM case only), and the square symbol marks the start of a more rapid tail off; these spectral locations may be interpreted as the limits of pre- and far-dissipation subranges (see text).

scaling varying as f^{-1} since a ratio of order 10 can be expected between eddy scales at mid-latitude and in the 2–6°N band.

The cycle of energy injection, transfer and dissipation for all solutions is presented in Fig. 13. KE injection (top panel) has a similar spectral profile at all resolutions but is weaker in the COARSE solution, contributing to its weaker KE (Fig. 10). At all resolutions, injection peak is situated near the transition point between forward and inverse KE cascade, *i.e.*, around the 600 km wavelength (middle panel). Note that the scale at which this transition occurs is also stable with resolution as previously observed. However, Π does not reach a plateau in the COARSE solution while the FINE and MEDIUM solutions have similar patterns up to the MEDIUM dissipation range. Likewise, the COARSE solution may have a KE injection deficit as a result of a wide lateral dissipation range (bottom panel). Note that vertical dissipation at all resolutions (not shown) mirrors, with opposite sign, the spectral pattern of KE injection in the submesoscale range, as shown for the MEDIUM resolution budget (Fig. 11).

Following the method of Skamarock (2004), we estimate the dissipation range and effective resolution of the model by identifying the high wavenumber portion of the KE spectrum where the curve shows a steep decay (exponential tail off). This method gives 30 km, 60 km and 210 km, respectively for the FINE, MEDIUM and COARSE solutions, *i.e.*, about $7\delta x$. These values may be thought of

as the effective ROMS resolution which has a similar dependency to grid-scale δx as found by Skamarock (2004) for the Weather Research and Forecast (WRF) model. This would explain that in the COARSE solution, the model dissipation range prevents the formation of submesoscale instabilities since the model effective resolution is coarser in this case than the dominant scales of MLI. However, inspection of the KE dissipation terms (Fig. 13, bottom panel) suggests that the dissipation range starts at even larger scales than estimated with the "Skamarock" method, *i.e.*, ~450 km, 200 km, and 80 km respectively. Therefore, the $7\delta x$ empirical law may be indicative of the far-dissipation range where energy decays exponentially (Martinez et al., 1997), but our results support the existence of a pre-dissipation range where dissipation is mild (below its maximum) but not negligible. It would explain why the k^{-2} slopes in MEDIUM and FINE solutions are interrupted at scales well above the dissipation maximum. The COARSE dissipation is not even clearly reduced at the largest scales, which would contribute to the COARSE solution having both weaker energy injection and weaker energy at all represented scales.

An alternative way of understanding how dissipation may work in spectral space is to consider that frontal structures project onto a large range of scales, when Fourier transformed, not just near the frontal scale. Therefore, dissipation acting on a front actually affects the full spectral range involved in the representation of that
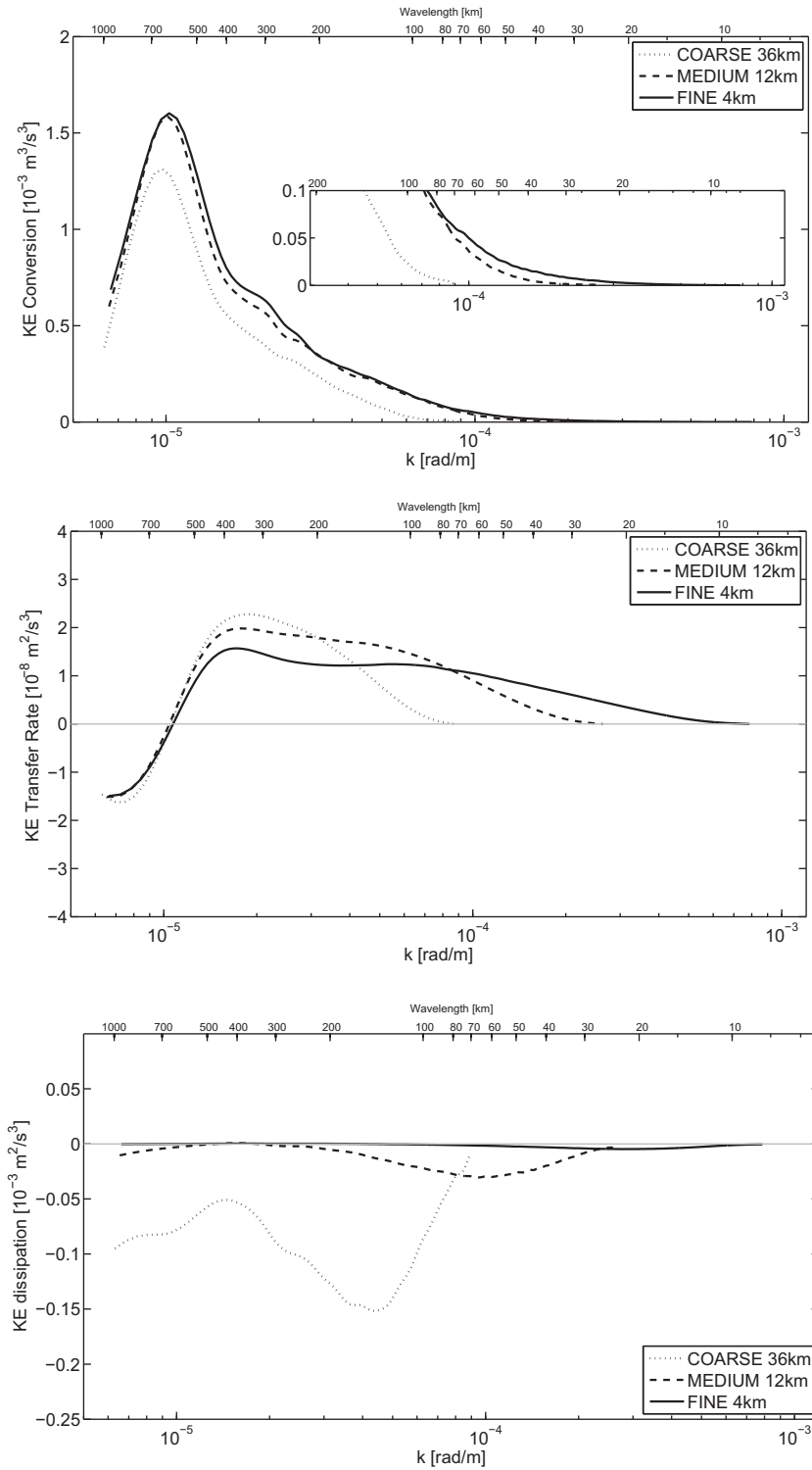
Fig. 13. Top: spectra of KE injection (top; 10^{-3} m^3/s^3), transfer rate (middle; 10^{-8} m^2/s^3) and lateral dissipation (bottom; 10^{-3} m^3/s^3) in the FINE, MEDIUM and COARSE solutions; the spectra are averaged over the TIW season and the mixed layer. In the inset of the top panel, KE injection spectra for high wavenumbers are plotted in a different scale to highlight differences between MEDIUM and FINE solutions.

front, from the mesoscale where the initial frontal deformation occurs down to the actual frontal scale.

3.6. Restratification

The equatorial heat budget has often been investigated for its relevance to ocean climate variability (Menkes et al., 2006) but the effect of small-scale dynamics on this budget has not been evaluated. As shown by Boccaletti et al. (2007), the main impact of submesoscale activity (whether related to mesoscale stirring or frontal instabilities) is restratification of the boundary layer through vertical buoyancy or temperature fluxes F_T:

$$F_T = -\frac{\partial \overline{w''T''}}{\partial z}. \tag{8}$$
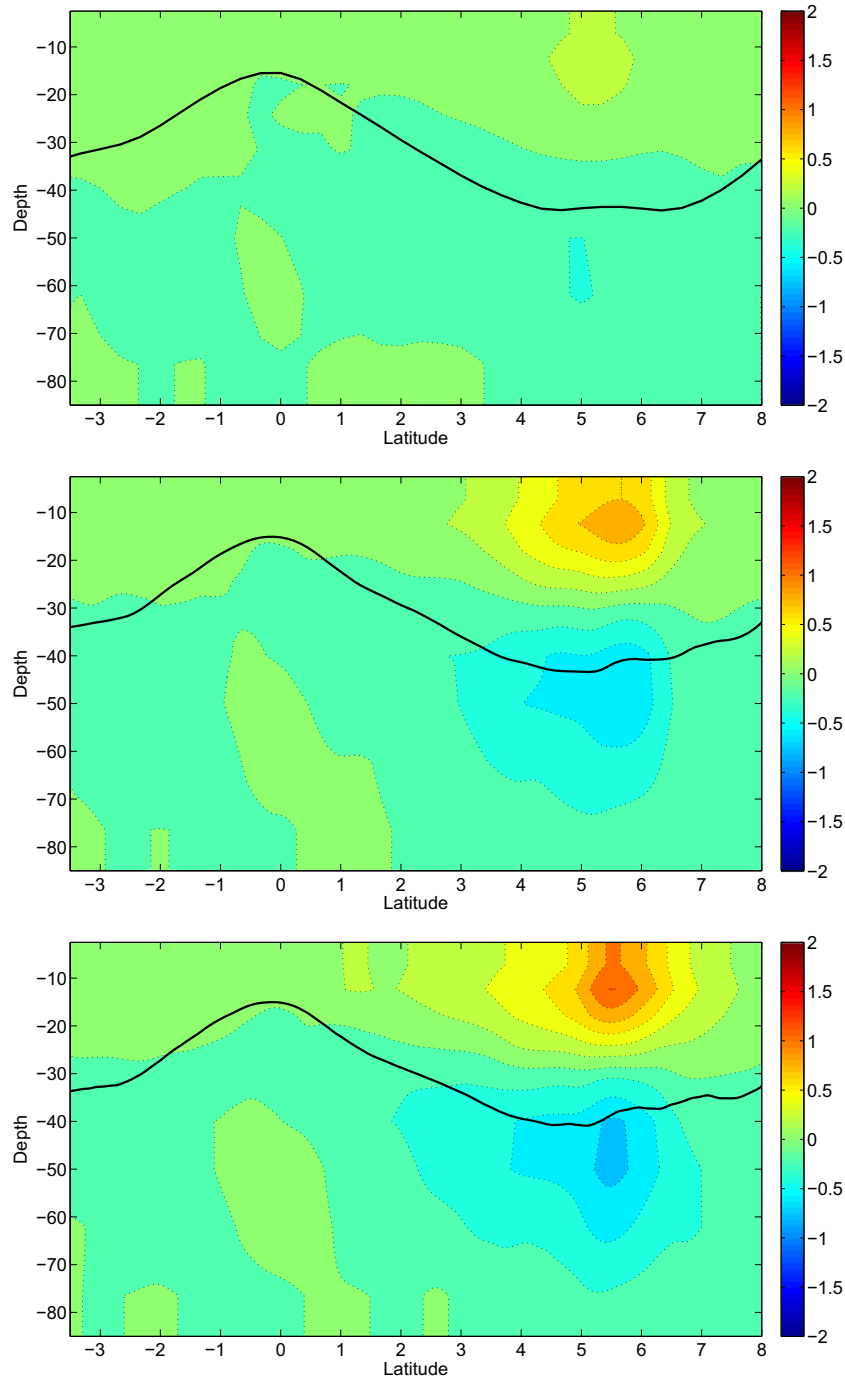
Fig. 14. Meridional section of temperature tendency (K/month) due to submesoscale vertical transport (Eq. (8)) in the FINE (bottom), MEDIUM (middle) and COARSE (top) solutions for the high TIW season. The black lines are the zonally averaged depth of the surface boundary layer.

Fig. 14 presents a zonal average of F_T for the three solutions at different resolutions. Maximum absolute values are about 1 K/month, which is of the order of lateral advection by TIWs (Jochum et al., 2007). The restratification process, with its vertical dipole pattern of warming and cooling, is apparent at all resolutions but increases in strength as resolution increases. The main area of restratification is located between 1°N and 8°N and centered around 5°N. This is also the area where submesoscale eddy kinetic energy (EKE) is found (Fig. 15, top panel). In the high resolution runs, EKE is much larger and explains the similar increase in F_T. Between the MEDIUM and FINE solutions, as in the previous analyses, we find relatively small differences in both EKE and F_T. However, we also notice that the differences between the two solutions tend to increase with latitude. In fact, the large values of *EKE* found between 6–8°N in the FINE solution coincide with the presence of submesoscale meanders and eddies that are weaker or absent in the other solutions (Fig. 8).

The length scale corresponding to mixed layer eddies (MLEs) is given by a so-called mixed layer deformation radius (Boccaletti et al., 2007) defined as NH/f, where N is the Brunt–Vaisala frequency in the mixed layer (small by definition and with little geographic variation), H the mixed layer depth and f the Coriolis parameter which is a sinus function of latitude ($f = 2\Omega \sin \phi$, Ω is angular speed of the Earth, ϕ is latitude). The MLE length scale
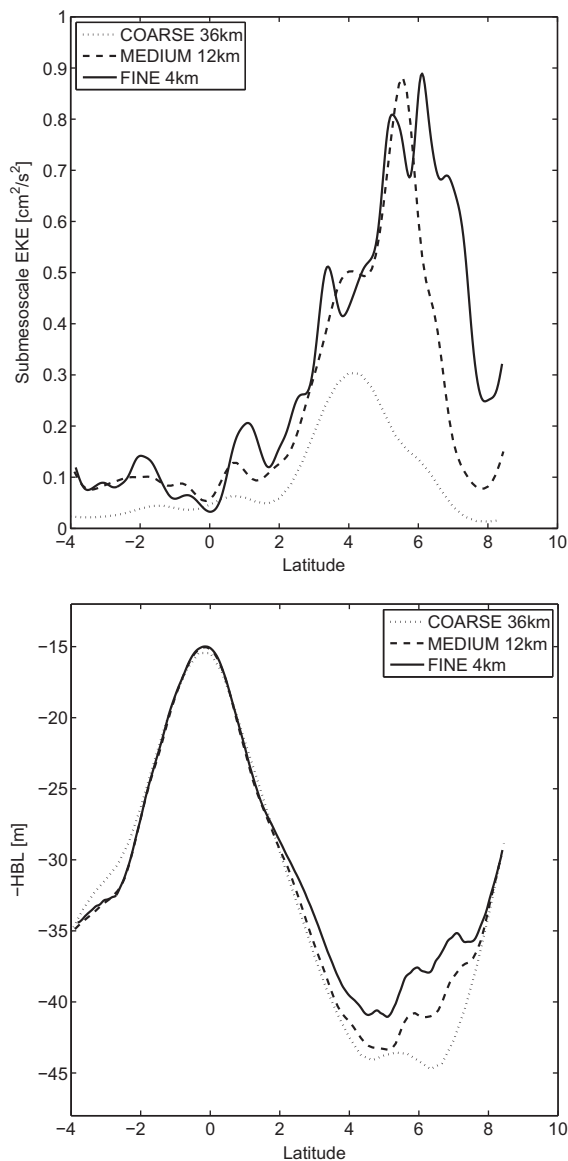
Fig. 15. Submesoscale EKE at 10 m (top), and boundary layer depth HBL (bottom) in the FINE, MEDIUM and COARSE solutions. EKE is computed as $\frac{1}{2}(u''^2 + v''^2)$ where u'' and v'' are high pass filtered with the operator described in Section 3.2. All fields are time averaged over the high TIW season and zonally averaged over longitudes 132–120°W.

should thus behave as an inverse function of latitude, although there is as yet no modeling or observational evidence of this dependence. In our simulations, typical wavelength of submesoscale meanders arise at 50–200 km, which is an order of magnitude larger than those generated at mid-latitude (10–20 km) and thus consistent with the f^{-1} MLE length scaling. Following this law, the size of MLEs should decrease rapidly with latitude away from the equator. At 6°N, it is around 90 km so that only the FINE solution (30–100 km effective resolution) may be able to properly resolve submesoscale turbulence in the 6–8°N latitude band.

Most importantly, Fig. 14 suggests that the presence of finer and better resolved eddy structures keeps modifying the surface heat balance until horizontal resolution has reached about 10 km. As a result of increased submesoscale restratification, the deepening of the boundary layer induced by TIV stretching around 5°N is partially compensated when cross-frontal circulations are at work (Fig. 14, overimposed black line; and Fig. 15, bottom panel). These effects remain necessarily small in our model because a restoring

term modifies the applied air-sea flux to maintain SST close to large-scale observations. We may expect larger sensitivities using less constrained, more realistic surface forcing, which would impact on the observed strong coupling between the atmosphere and the ocean surface (Chelton et al., 2001). Note that our reasoning assumes that surface mesoscale activity itself is not overly altered by submesoscale dynamics (through upscaling effects) which could otherwise modify the heat budget in deeper ways. Nevertheless, and even though our submesoscale solutions are for a restricted subregion of the central Pacific, they support the idea that submesoscale upscaling effects are indeed rather weak.

4. Discussion and conclusion

In this paper, the submesoscale-resolving model used in mid-latitude by Capet et al. (2008c) was applied to the near equatorial region of central Pacific where tropical instability waves are the dominant "mesoscale" phenomena. A suite of model solutions with increasing resolution shows that the conventional mid-latitude KE spectrum is in this case strongly shifted towards larger scales with a magnitude consistent with a latitudinal dependence of eddy scales. As a consequence of the general shift of eddy length scales, the resolution convergence of KE spectrum in TIWs is achieved with a grid mesh size of 12 km, and is manifested in both energy injection and spectral energy fluxes at the submesoscale range. It implies that mesoscale dynamics associated with TIWs and their impact on the equatorial upwelling are almost fully captured at about 10 km resolution. However, the restratification process by mixed layer eddies is not fully captured at this resolution, in particular in the northern area of TIWs where these eddies are vigorous. Yet, MLI perturbations with wavelengths as large as 50–200 km instead of 10–20 km at mid-latitude develop at a model resolution of 12 km, instead of 1 km. Here again, the differences agree with a f^{-1} law of MLE scaling using the mixed layer deformation radius. This result is of importance to applications of MLI parametrization in global models (Fox-Kemper et al., in press).

TIWs are a major contributor to the heat and biogeochemical balance of the equatorial upwelling region (Hansen and Paul, 1984; Gorgues et al., 2005). Mid-latitude submesoscale-resolving simulations tend to show that lateral heat (or buoyancy) flux is dominated by mesoscale eddies, while vertical buoyancy flux is dominated by submesoscale dynamics (Capet et al., 2008b). This general statement appears to be true also for TIWs. It was already known that the effect of instability waves (at the wave scale) is a warming of the equatorial cold tongue through meridional exchanges with tropical waters (Baturin and Niiler, 1997; Menkes et al., 2006); in the present study, the TIW submesoscale effect, as in mid-latitude region, is to restratify the mixed layer (which sees as much as 20% height reduction around 6°N). MLEs appear particularly efficient in this process as suggested by the comparison between MEDIUM and FINE solutions. Addressing more precisely the submesoscale effects on heat and biogeochemical budgets should be considered in future studies.

A relevant aspect of our results for ocean modeling is the spectral decomposition of subgrid-scale dissipation. It is often assumed in oceanography that hyperviscous operators (high-order filters) are useful artifacts to avoid "wasting resolution" by dissipating scales around the mesh size (Frisch et al., 2008, for a critical review). The use of high-order filters are only appropriate in conjunction with high-order discretization methods with low dispersion errors (Durran, 2010). Therefore, in practice, additional filters (spatial or temporal) to hyperviscous operators are often needed. Skamarock (2004) has provided a simple way of estimating the range of scales that can be effectively modified by model dissipation. It concerns not only the viscous operator but more generally

the ensemble of numerical filters used in the model (Durran, 1991, for the Robert-Asselin temporal filter example). In regional models with high-order schemes, such as ROMS or WRF, both numerical dispersion and dissipation are reduced to increase the effective resolution at a given mesh size; in this case, according to the method of Skamarock (2004), the model effective resolution is estimated between 5–10 δx. However, our spectral decomposition of KE lateral dissipation (an equivalent biharmonic operator with velocity dependent viscosity) provides new insight which shows that dissipation can be farther reaching than estimated from the KE spectra alone. When hyperviscosity is used, as here, the far-dissipation range may well be made closer to the grid scale ($D_H(k) \propto k^4 E(k)$ instead of $k^2 E(k)$) but the advantage of widening the quasi-inertial range may be partly offset by the maintenance of an intermediate spectral region where dissipation may be mild but not negligible (Frisch et al., 2008). As a result, MEDIUM and FINE solutions have their submesoscale k^{-2} slopes interrupted at scales well above the dissipation maximum (in the far-dissipation range), and the COARSE solution presents an energy deficit at all represented scales. Note that in the pre-dissipation range, KE seems to decay as k^{-3} (Fig. 10) but this is not confirmed by the compensated spectrum $k^3 E(k)$ (not shown); a fake impression of QG inertial enstrophy cascade may thus be conveyed by excessive numerical dissipation.

The embedded approach with 2-way nesting communication, available in the AGRIF version of ROMS, has proven here very useful to address small scale phenomena and analyze their resolution sensitivity at relatively low computational cost (and with little burden of building configurations). A large part of the success is in the techniques developed by Debreu et al. (2011), preserving conservation and continuity at the grids interface. However, there is a downside of using smaller regional domains for spectral decomposition as windowing or periodization methods can reach their limits of validity (Denis et al., 2002). In our case, we noticed a budget residual at large scale (above 300 km) which can be attributed to both offline computation and spectral analysis errors. For this reason, we systematically checked the consistency of our results on various domains and resolutions and ensured at least that our analysis provides a robust, if not exact, interpretation of underlying dynamics. Another caveat is the limited statistical reliability of our solutions at the TIW scale over only 3 months during which the temporal tendency is not negligible. More reliability would be achieved by multiple years of simulation. Nevertheless, we believe that the results will remain qualitatively similar.

Acknowledgments

References

Baturin, N.G., Niiler, P.P., 1997. Effects of instability waves in the mixed layer of the equatorial pacific. Journal of Geophysical Research 102 (C13), 27771–27793.

Boccaletti, G., Ferrari, R., Fox-Kemper, B., 2007. Mixed layer instabilities and restratification. Journal of Physical Oceanography 37 (9), 2228–2250.

Capet, X., McWilliams, J.C., Molemaker, M.J., Shchepetkin, A.F., 2008a. Mesoscale to submesoscale transition in the california current system. Part I: flow structure, eddy flux, and observational tests. Journal of Physical Oceanography 38 (1), 29–43.

Capet, X., McWilliams, J.C., Molemaker, M.J., Shchepetkin, A.F., 2008b. Mesoscale to submesoscale transition in the california current system. Part II: frontal processes. Journal of Physical Oceanography 38 (1), 44–64.

Capet, X., McWilliams, J.C., Molemaker, M.J., Shchepetkin, A.F., 2008c. Mesoscale to submesoscale transition in the california current system. Part III: energy balance and flux. Journal of Physical Oceanography 38 (10), 2256–2269.

Chelton, D.B., Esbensen, S.K., Schlax, M.G., Thum, N., Freilich, M.H., Wentz, F.J., Gentemann, C.L., McPhaden, M.J., Schopf, P.S., 2001. Observations of coupling between surface wind stress and sea surface temperature in the eastern tropical pacific. Journal of Climate 14 (7), 1479–1498.

Couvelard, X., Marchesiello, P., Gourdeau, L., Lefèvre, J., 2008. Barotropic zonal jets induced by islands in the southwest pacific. Journal of Physical Oceanography 38 (10), 2185–2204.

Cravatte, S., Menkes, C., 2009. Sensitivity of mixed layer heat budgets to wind forcing: a case study for the equatorial pacific cold tongue. Ocean Modelling 29 (3), 198–212.

da Silva, A.M., Young, C.C., Levitus, S., 1994. Atlas of surface marine data 1994. Tech. Rep. NOAA/NESDIS Atlases 6-10, U.S. Department of Commerce, NOAA, NESDIS.

Davidson, P.A., 2004. Turbulence: An Introduction for Scientists and Engineers. Oxford University Press.

Debreu, L., Marchesiello, P., Penven, P. Two-way embedding algorithms for a split-explicit free surface model. Ocean Modeling, submitted for publication.

Denis, B., Côté, J., Laprise, R., 2002. Spectral decomposition of two-dimensional atmospheric fields on limited-area domains using the discrete cosine transform (DCT). Monthly Weather Review 130, 1812–1829.

Durran, D.R., 1991. The third-order adams-bashforth method – an attractive alternative to leapfrog time differencing. Monthly Weather Review 119, 702–720.

Durran, D.R., 2010. Numerical Methods for Fluid Dynamics: With Applications to Geophysics. Texts in Applied Mathematics, vol. 32. Springer.

Flament, P., Kennan, S.C., Knox, R., Niiler, P.P., Bernstein, R., 1996. The three-dimensional structure of an upper vortex in the tropical pacific. Nature 383, 610–613.

Fox-Kemper, B., Danabasoglu, G., Ferrari, R., Griffies, S., Hallberg, R., Holland, M., Maltrud, M., Peacock, S., Samuels, B. Parameterization of mixed layer eddies. iii: Implementation and impact in global ocean climate simulations. Ocean Modelling, in press.

Frisch, U., Kurien, S., Pandit, R., Pauls, W., Ray, S., Wirth, A., Zhu, J., 2008. Hyperviscosity, Galerkin truncation, and bottlenecks in turbulence. Physical Review Letters 101 (14).

Garrett, C.J.R., Loder, J.W., 1981. Dynamical aspects of shallow sea fronts. Philosophical Transactions of the Royal Society of London. Series A, Mathematical and Physical Sciences 302 (1472), 563–581.

Gorgues, T., Menkes, C., Aumont, O., Vialard, J., Dandonneau, Y., Bopp, L., 2005. Biogeochemical impact of tropical instability waves in the equatorial pacific biogeochemical impact of tropical instability waves in the equatorial pacific. Geophysical Research Letters 32 (L24615), 4.

Hansen, D.V., Paul, C.A., 1984. Genesis and effects of long waves in the equatorial pacific. Journal of Geophysical Research 89 (C6), 10431–10440.

Hoskins, B.J., 1982. The mathematical theory of frontogenesis. Annual Review of Fluid Mechanics 14, 131–151.

Jochum, M., Cronin, M.F., Kessler, W.S., Shea, D., 2007. Observed horizontal temperature advection by tropical instability waves. Geophysical research Letters 34 (L09604), 4.

Johnson, E.S., 1996. A convergent instability wave front in the central tropical pacific. Deep Sea Research Part II: Topical Studies in Oceanography 43 (4–6), 753–778.

Kennan, S.C., Flament, P.J., 2000. Observations of a tropical instability vortex. Journal of Physical Oceanography 30 (9), 2277–2301.

Klein, P., Hua, B.L., Lapeyre, G., Capet, X., Sylvie, L.G., Sasaki, H., 2008. Upper ocean turbulence from high-resolution 3d simulations. Journal of Physical Oceanography 38 (8), 1748–1763.

Large, W.G., McWilliams, J.C., Doney, S.C., 1994. Oceanic vertical mixing: a review and a model with a nonlocal boundary layer parameterization. Reviews of Geophysics 32, 363–403.

Legeckis, R., 1986. A satellite time series of sea surface temperatures in the eastern equatorial pacific ocean, 1982–1986. Journal of Geophysical Research 91 (C11), 12879–12886.

Le Traon, P.Y., Klein, P., Hua, B.L., Dibarboure, G., 2008. Do altimeter wavenumber spectra agree with the interior or surface quasigeostrophic theory? Journal of Physical Oceanography 38 (5), 1137–1142.

Lumpkin, R., Garraffo, Z., 2005. Evaluating the decomposition of tropical atlantic drifter observations. Journal of Atmospheric and Oceanic Technology 22 (9), 1403–1415.

Luther, D.S., Johnson, E.S., 1990. Eddy energetics in the upper equatorial pacific during the hawaii-to-tahiti shuttl experiement. Journal of Physical Oceanography 20 (7), 913–944.

Lyman, J.M., Johnson, G.C., Kessler, W.S., 2007. Distinct 17- and 33-day tropical instability waves in subsurface observations. Journal of Physical Oceanography 37 (4), 855–872.

Marchesiello, P., McWilliams, J.C., Shchepetkin, A., 2001. Open boundary conditions for long-term integration of regional oceanic models. Ocean Modelling 3 (1–2), 1–20.

Marchesiello, P., Debreu, L., Couvelard, X., 2009. Spurious diapycnal mixing in terrain-following coordinate models: the problem and a solution. Ocean Modelling 26 (3–4), 156–169.

Martinez, D.O., Chen, S., Doolen, G.D., Kraichnan, R.H., Wang, L.-P., Zhou, Y., 1997. Energy spectrum in the dissipation range of fluid turbulence. Journal of Plasma Physics 57 (01), 195–201.

Masina, S., Philander, S.G.H., Bush, A.B.G., 1999. An analysis of tropical instability waves in a numerical model of the Pacific ocean 2. Generation and energetics of the waves. Journal of Geophysical Research 104 (C12), 29637–29661.

McPhaden, M.J., McCarty, M.E., 1992. Mean seasonal cycles and interannual variations at 0,110w and 0,140w during 1980–1991. Tech. memo, NOAA, ERL PMEL-95, U.S. Department of Commerce, Washington, DC.

Menkes, C.E.R., Vialard, J.G., Kennan, S.C., Boulanger, J.-P., Madec, G.V., 2006. A modeling study of the impact of tropical instability waves on the heat budget of the eastern equatorial Pacific. Journal of Physical Oceanography 36 (5), 847–865.

Molemaker, M.J., McWilliams, J.C.M., Capet, X., 2010. Balanced and unbalanced routes to dissipation in an equilibrated eady flow. Journal of Fluid Mechanics 654, 35–63.

Murray, J.W., Barber, R.T., Roman, M.R., Bacon, M.P., Feely, R.A., 1994. Physical and biological controls on carbon cycling in the equatorial Pacific. Science 266 (5182), 58–65.

Niiler, P.P., 1969. On the ekman divergence in an oceanic jet. Jouranl of Geophysical Research 74, 7048–7052.

Penven, P., Debreu, L., Marchesiello, P., McWilliams, J.C., 2006. Evaluation and application of the roms 1-way embedding procedure to the central California upwelling system. Ocean Modelling 12 (1–2), 157–187.

Penven, P., Marchesiello, P., Debreu, L., Lefèvre, J., 2008. Software tools for pre- and post-processing of oceanic regional simulations. Environmental Modelling and Software 23 (5), 660–662.

Scott, R.B., Wang, F., 2005. Direct evidence of an oceanic inverse kinetic energy cascade from satellite altimetry. Journal of Physical Oceanography 35 (9), 1650–1666.

Scott, R., Xu, Y., 2009. An update on the wind power input to the surface geostrophic flow of the World ocean. Deep Sea Research Part I 56 (3), 295–304.

Seo, H., Jochum, M., Murtugudde, R., Miller, A.J., Roads, J.O., 2007. Feedback of tropical instability-wave-induced atmospheric variability onto the ocean. Journal of Climate 20 (23), 5842–5855.

Shchepetkin, A.F., McWilliams, J.C., 1998. Quasi-monotone advection schemes based on explicit locally adaptive dissipation. Monthly Weather Review 126 (6), 1541–1580.

Shchepetkin, A.F., McWilliams, J.C., 2003. A method for computing horizontal pressure-gradient force in an oceanic model with a nonaligned vertical coordinate. Journal of Geophysical Research 108, 3090–30124.

Shchepetkin, A.F., McWilliams, J.C., 2005. The regional oceanic modeling system (roms): a split-explicit, free-surface, topography-following-coordinate oceanic model. Ocean Modelling 9 (4), 347–404.

Skamarock, W.C., 2004. Evaluating mesoscale nwp models using kinetic energy spectra. Monthly Weather Review 132 (12), 3019–3032.

Smith, S., 2007. The geography of linear baroclinic instability in earth's oceans. Journal of Marine Research 65, 655–683.

Stern, M.E., 1965. Interaction of a uniform wind stress with a geostrophic vortex. Deep Sea Research and Oceanographic Abstracts 12 (3), 355–367.

Taylor, J.R., Ferrari, R., 2009. On the equilibration of a symmetrically unstable front via a secondary shear instability. Journal of Fluid Mechanics 622, 103–113.

Thomas, L.N., Lee, C.M., 2005. Intensification of ocean fronts by down-front winds. Journal of Physical Oceanography 35 (6), 1086–1102.

Thomas, L.N., Tandon, A., Mahadevan, A., 2008. Submesoscale processes and dynamics. In: M.W., Hecht, H., Hasumi, (Eds.), Ocean Modeling in an Eddying Regime. Geophysical Monograph series, American Geophysical Union, vol. 177, pp. 17–38.

Tulloch, R., Marshall, J., Hill, C., Smith, K.S., in press. Scales, growth rates and spectral fluxes of baroclinic instability in the ocean. Journal of Physical Oceanography.

Vialard, J., Menkes, C., Boulanger, J.-P., Delecluse, P., Guilyardi, E., McPhaden, M.J., Madec, G., 2001. A model study of oceanic mechanisms affecting equatorial pacific sea surface temperature during the 1997–98 el niño. Journal of Physical Oceanography 31 (7), 1649–1675.

Willett, C.S., Leben, R.R., Lavín, M.F., 2006. Eddies and tropical instability waves in the eastern tropical pacific: a review. Progress In Oceanography 69 (2–4), 218–238 (a review of Eastern Tropical Pacific Oceanography).

Yoder, J.A., Ackleson, S.G., Barber, R.T., Flament, P., Balch, W.M., 1994. A line in the sea. Nature 371, 689–692.